Journal of The Electrochemical Society, **150** (4) A508-A519 (2003)
0013-4651/2003/150(4)/A508/12/$7.00 © The Electrochemical Society, Inc.

Mathematical Modeling of Liquid-Feed Direct Methanol Fuel Cells

Z. H. Wang* and C. Y. Wang*,z

Electrochemical Engine Center and Department of Mechanical and Nuclear Engineering, The Pennsylvania State University, University Park, Pennsylvania 16802, USA

A two-phase, multicomponent model has been developed for liquid-feed direct methanol fuel cells (DMFC). In addition to the anode and cathode electrochemical reactions, the model considers diffusion and convection of both gas and liquid phases in the backing layers and flow channels. In particular, the model fully accounts for the mixed potential effect of methanol oxidation at the cathode as a result of methanol crossover caused by diffusion, convection, and electro-osmosis. This comprehensive model is solved numerically using computational fluid dynamics. The transport phenomena and electrochemical kinetics in a liquid-feed DMFC are delineated and the effects of the methanol feed concentration on cell performance are explored. The model is validated against DMFC experimental data with reasonable agreement. The void fraction at the anode outlet is found to be as high as 95% at a cell current density of 0.45 A/cm^2 for a 7 cm long channel. Increase in methanol feed concentration leads to a slight decrease in cell voltage and a proportional increase in the mass-transport limiting current density for a methanol concentration below 1 M. However, when the methanol feed concentration is larger than 2 M, the cell voltage is greatly reduced by excessive methanol crossover and the maximum current density begins to be limited by the oxygen supply at the cathode. The oxygen depletion results from excessive parasitic oxygen consumption by methanol crossing over.
 [DOI: 10.1149/1.1559061]

Manuscript submitted July 22, 2002; revised manuscript received September 19, 2002. Available electronically March 4, 2003.

Fuel cells promise to replace the internal combustion engine in transportation due to their higher energy efficiency and zero or ultralow emissions, and to replace batteries for portable electronics due to potentially higher energy density and nearly zero recharge time. Hydrogen proton exchange membrane fuel cells (PEMFC) and liquid-feed direct methanol fuel cells (DMFC) are presently considered as two potential types of fuel cells for such applications. Compared to hydrogen PEMFC, DMFC has further advantages of easier fuel delivery and storage, no cooling or humidification needs, and simpler design.

However, the wide application of DMFC is still hindered by several technological problems, low electro-activity of methanol oxidation on the anode, substantial methanol crossover through the polymer membrane, and severe cathode flooding. The cell performance is limited by anode kinetics due to its low exchange current density and high Tafel slope.[1] Methanol crossover further causes lower open-circuit voltage (OCV) and waste of fuel and hence lower energy conversion efficiency. Water management greatly influences the cathode performance.[2,3]

Much work has been focused on the anodic oxidation of methanol.[2] The mechanism of the electrocatalytic oxidation of methanol at the anode was postulated.[3,4] Different anode catalyst structures of Pt-Ru were developed,[5] and several anode catalysts other than Pt-Ru were explored.[6-8] Additionally, the effects of the anode electrochemical reaction on cell performance were experimentally studied.[9-11]

Methanol crossover in DMFC has been extensively studied both experimentally and theoretically. Narayanan *et al.*[12] and Ren *et al.*[13] measured the methanol crossover flux with different membrane thicknesses and showed that the methanol crossover rate is inversely proportional to the membrane thickness at a given cell current density, thus indicating that diffusion is dominant. In addition, Ren *et al.*[14] compared the diffusion with electro-osmotic drag processes and demonstrated the importance of the electro-osmotic drag in the methanol transport through the membrane. In their analysis, the methanol electro-osmotic drag is considered as a convection effect and the diluted methanol moves with electro-osmotically dragged water molecules. Tricoli *et al.*[15] compared the methanol transport in two types of membranes. Valdez and Narayanan[16] studied the temperature effects on methanol crossover and showed that the methanol crossover rate increases with cell temperature. Hikita *et al.*[17] measured methanol crossover and cell performance under different membrane thickness and methanol feed concentrations. Their experiments showed that the cell performance during operation is affected by methanol crossover but not significantly dependent on methanol crossover flux in the case of sufficient oxygen supply. Ravikumar and Shukla[11] operated the liquid-feed DMFC at the oxygen pressure of 4 bars and found that the cell performance is greatly affected by methanol crossover at the methanol feed concentration greater than 2 M, and that this effect aggravates with the operating temperature. Wang *et al.*[18] analyzed the chemical compositions of the cathode effluent of a DMFC with a mass spectrometer. They found that the methanol crossing over the membrane is completely oxidized to CO_2 at the cathode in the presence of a Pt catalyst. Additionally, the cathode potential is influenced by the mixed potential phenomenon due to simultaneous methanol oxidation and oxygen reduction as well as poisoning of Pt catalysts by methanol oxidation intermediates. Kauranen and Skou[19] presented a semi-empirical model to describe the methanol oxidation and oxygen reduction reactions on the cathode and concluded that the oxygen reduction current is reduced in the presence of methanol oxidation due to surface poisoning.

In spite of these challenges, progress in the DMFC performance has been made steadily by many groups, *e.g.*, Halpert *et al.*[20] of Jet Propulsion Laboratory (JPL) and Giner, Inc., Baldauf and Preidel[21] of Siemens, Ren *et al.*[22] of Los Alamos National Laboratory (LANL), and Mench *et al.*,[23,24] and Lim and Wang[51] of the Penn State University. A comparative study of DMFC with hydrogen PEMFC was presented most recently by the LANL group.[25,26]

While attempts are continuing to elucidate the fundamental electrochemical reaction mechanisms, to explore new compositions and structures of catalysts, and to develop new membranes and methods for preventing methanol crossover, important system issues on DMFC are emerging, such as water management, gas management, flow field design and optimization, and cell up-scaling for different applications. A number of physicochemical phenomena take place in liquid-feed DMFC, including species, charge, and momentum transfer, multiple electrochemical reactions, and gas-liquid two-phase flow in both anode and cathode. Carbon dioxide evolution in the liquid-feed anode results in strongly two-phase flow, making the processes of reactant supply and product removal more complicated. All these processes are intimately coupled, resulting in a need to search for optimal cell design and operating conditions. A good understanding of these complex, interacting phenomena is thus es-

* Electrochemical Society Active Member.
z E-mail: cxw31@psu.edu

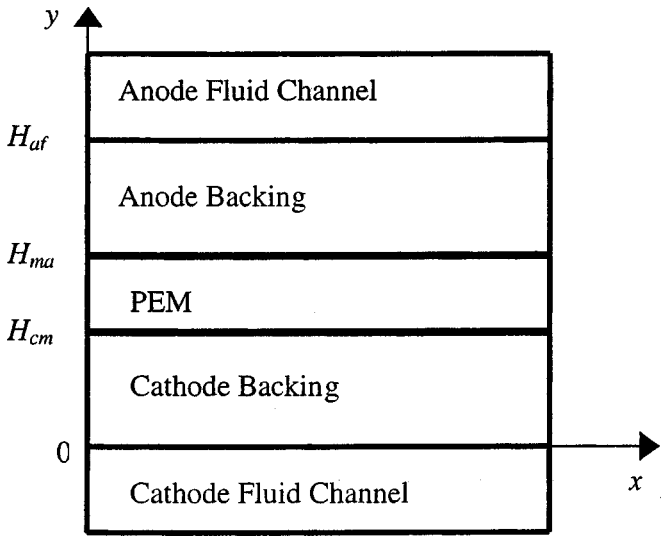

Figure 1. Schematic of a liquid-feed direct methanol fuel cell and the coordinate system for the present model.

sential and can be most likely achieved through a combined mathematical modeling and detailed experimental approach.

Baxter *et al.*[27] developed a one-dimensional mathematical model for a liquid-feed DMFC, mainly focused on the anode catalyst layer. A major assumption of their study was that the carbon dioxide is only dissolved in the liquid and hence their model of transport and electrochemical processes in the anode catalyst layer is single-phase only. Using a macrohomogeneous model to describe the reaction and transport in the catalyst layer of vapor-feed anode, Wang and Savinell[28] discussed the effects of the anode catalyst layer structure on cell performance. Kulikovsky *et al.*[29] simulated a vapor-feed DMFC with a two-dimensional model and compared the detailed current density distributions in backing, catalyst layer, and membrane separator between conventional and alternative current collectors. In another paper, Kulikovsky[30] numerically studied a liquid-feed DMFC considering methanol transport through the liquid phase and in hydrophilic pores of the anode backing. In both publications of Kulikovsky, the important phenomenon of methanol crossover was ignored. Dohle *et al.*[31] presented a one-dimensional model for the vapor-feed DMFC, and the crossover phenomenon was described. The effects of methanol concentration on the cell performance were studied. Scott *et al.*[32-35] also developed several simplified single-phase models to study transport and electrochemical processes in liquid-feed DMFC and showed that the cell performance is limited by the slow diffusion of methanol in liquid.

In this paper, a comprehensive model for two-phase flow, multicomponent transport, and detailed electrochemical reactions is presented for a liquid-feed DMFC, including electrodes, channels, and PEM separator. The model is intended to provide a useful tool for the basic understanding of transport and electrochemical phenomena in DMFC and for the optimization of cell design and operating conditions. The model is solved using computational fluid dynamics (CFD) and validated against experimental performance data. The multidimensional transport and electrochemical processes are numerically analyzed and the effects of the anode feed methanol concentration on cell performance are studied in detail to illustrate the utility of the present model. The two-phase transport in anode and cathode, methanol crossover, as well as their effects on cell performance are explored.

Mathematical Modeling

Consider a two-dimensional direct methanol fuel cell as schematically illustrated in Fig. 1. The fuel cell includes a fluid channel, a backing layer, and a catalyst layer in both electrodes, and a membrane separator between the two electrodes. In the present model, the catalyst layers are simplified as infinitely thin interfaces between the backing layer and membrane separator where the following two electrochemical reactions take place

$$CH_3OH + H_2O \rightarrow CO_2 + 6H^+ + 6e \quad [1]$$

$$O_2 + 4H^+ \rightarrow 2H_2O - 4e \quad [2]$$

At the anode catalyst layer, methanol is oxidized via Eq. 1 while both oxygen reduction and methanol oxidation take place at the cathode via Eq. 2 and 1, respectively. According to the vast experimental evidence,[18] methanol crossing over is virtually totally oxidized at the cathode catalyst layer. The parasitic methanol oxidation reduces the cathode potential as can be explained as short circuit in the cathode catalyst layer. The above electrochemical reactions can be summarized generally as

$$\sum_k S_{Ri}^k M_k^{z_k} = n_{Ri} e^- \quad [3]$$

where k, M_k, S^k, z_k, and n_{Ri} represent species k, chemical formula of species k, stoichiometric coefficient, charge number of species k, and the total number of electrons produced in Reaction 1, respectively. The values of n_{Ri} are equal to 6 for Reaction 1 and -4 for Reaction 2.

For the sake of mathematical modeling, a full cell can be divided into two main groups, porous regions and flow channels. The porous regions include the backing and catalyst layers of two electrodes and membrane separator. The two regions are described mathematically by different models. The two-phase mixture model developed for two-phase flow and transport in the porous air cathode[36] is extended herein for all the porous regions in the liquid-feed DMFC, while a drift flux model is used to describe the two-phase flow and transport in fluid channels. Both models are elaborated below.

Porous regions.—Governing equations.[36,37]

$$\frac{\partial(\varepsilon\rho)}{\partial t} + \nabla \cdot (\rho \mathbf{u}) = 0 \quad [4]$$

Momentum conservation

$$\mathbf{u} = -\frac{K}{\mu}(\nabla p + \rho_\kappa \mathbf{g}) + \frac{n_d M}{\rho}\frac{\mathbf{I}_e}{F} \quad [5]$$

Here the fluid velocity is caused by the pressure gradient, gravity, and electro-osmotic drag. The first term in Eq. 5 is the contribution of pressure gradient and gravity to the fluid velocity described by Darcy's law and applied for single- and two-phase flows in porous media while the second term is the contribution of electro-osmotic drag which is the sum of electro-osmotic drag fluxes of all the species, *i.e.*, H_2O, MeOH, and H^+ in DMFC. In the equation, M is the molecular weight of the membrane pore fluid mixture and n_d is the fluid drag coefficient, which can be expressed as, respectively

$$M = \sum_k x^k M^k \quad n_d = \frac{\sum_k n_d^k M^k}{M}$$

Considering the dilute nature of methanol aqueous solution, the average molecular weight, M, can be assumed equal to the water molecular weight and the fluid drag coefficient, n_d, equal to the drag coefficient of water in the membrane. In this case, the electro-osmotic drag of diluted methanol solution is considered equivalent to convection effects of electro-osmotically dragged water molecules as described by Ren *et al.*[14]

Species conservation

$$\frac{\partial}{\partial t}(\varepsilon\rho C^{k}) + \nabla\cdot(\gamma_c\rho\mathbf{u}C^{k}) = \nabla\cdot(\rho_l D^{k}_{l,\text{eff}}\nabla C^{k}_{l} + \rho_g D^{k}_{g,\text{eff}}\nabla C^{k}_{g}) - \nabla\cdot[(C^{k}_{l} - C^{k}_{g})\mathbf{j}_l] + \dot{m}^{k} \quad [6]$$

This general species conservation equation is applicable to methanol (CH_3OH), carbon dioxide (CO_2), oxygen (O_2), and water (H_2O). The first three terms describe the accumulation, convection, and diffusion of species k, respectively. The convection term includes the electro-osmotic drag effect, as evident for Eq. 5 where the fluid velocity is driven by not only the pressure gradient but also the electro-osmotic drag. The diffusion term consists of diffusion through the liquid and gas phases and the effective diffusion coefficients can be expressed as, respectively

$$D^{k}_{l,\text{eff}} = (\varepsilon s)^{t_l}D^{k}_{l} \quad D^{k}_{g,\text{eff}} = [\varepsilon(1-s)]^{t_g}D^{k}_{g} \quad [7]$$

Note that tortuosity values are assumed equal to unity, except for in the membrane which is assumed 1.8 based on the calculation of methanol crossover flux at open circuit in the present work.

The second term on the right of Eq. 6 represents species transfer caused by relative motion of liquid to gas phase under capillary action. In this term, the capillary-diffusional flux of the liquid phase, j_l, as defined in Eq. 21, is directly proportional to the gradient in capillary pressure, and thus is related to the wetting characteristics of the porous electrode structure.

The last term in Eq. 6 stands for the source/sink due to electrochemical reactions. On the anode catalyst layer, there is the methanol oxidation reaction that produces the cell current density, *I*. However, on the cathode, there are two simultaneous electrochemical reactions, oxidation of methanol crossing through the membrane and oxygen reduction. The oxygen reduction reaction current must provide not only the net cell current density (through the external circuit) but also the parasitic current density from methanol crossover, that is ($I + I_p$). It follows that $\dot{m}^k$ is given by

$$\dot{m}^{k} = \begin{cases} \dfrac{M^{k}}{F}\dfrac{S^{k}_{R1}}{n_{R1}}I & \text{at } y = H_{ma} \\ \dfrac{M^{k}}{F}\left[\dfrac{S^{k}_{R1}}{n_{R1}}I_p + \dfrac{S^{k}_{R2}}{n_{R2}}(I + I_p)\right] & \text{at } y = H_{cm} \end{cases} \quad [8]$$

The first expression on the right side of Eq. 8 describes the source/sink of species k on the anode catalyst layer, whereas the second expression stands for the source/sink on the cathode catalyst layer. Because of nearly complete oxidation of methanol at the cathode under the very large surface overpotential, the parasitic methanol current is dictated by the crossover rate, j^{MeOH}, as follows

$$I_p = -\frac{6Fj^{\text{MeOH}}|_{y=H_{cm}}}{M^{\text{MeOH}}} \quad [9]$$

where the methanol crossover flux is given by

$$j^{\text{MeOH}}|_{y=H_{cm}} = \left(\rho_l\nu_l C^{\text{MeOH}}_{l} - \rho D^{\text{MeOH}}_{l,\text{eff}}\frac{\partial C^{\text{MeOH}}_{l}}{\partial y}\right)\Bigg|_{y=H_{cm}} \quad [10]$$

The terms on the right side of Eq. 10 describe convection due to the pressure difference between anode and cathode chambers and electro-osmotic drag, as well as diffusion. It should be noted that since the convection term is a function of methanol concentration, the three contributions to the methanol crossover flux in Eq. 10, namely, convection by the pressure gradient, convection by the electro-osmotic drag, and diffusion by the concentration gradient, are calculated specifically at the anode backing/membrane interface. The two convection contributions are calculated via Eq. 5.

Finally, summation of Eq. 6 over all species k results in Eq. 4, the total mass balance. This is because $\Sigma_k\gamma_c C^k = 1$ in the convection term (see the definitions of γ_c and C^k below in Eq. 12 and 17), all interdiffusion terms cancel with each other, and the species capillary fluxes and reaction rates have the summation equal to zero.

Mixture parameters.—In the governing Eq. 4-6, the mixture variables and properties are defined as[36,37]

Density $$\rho = \rho_l s + \rho_g(1-s) \quad [11]$$

Concentration $$\rho C = \rho_l C_l s + \rho_g C_g(1-s) \quad [12]$$

Velocity $$\rho\mathbf{u} = \rho_l\mathbf{u}_l + \rho_g\mathbf{u}_g \quad [13]$$

Kinetic density $$\rho_\kappa = \rho_l\lambda_l(s) + \rho_g\lambda_g(s) \quad [14]$$

Viscosity $$\mu = \frac{\rho_l s + \rho_g(1-s)}{(k_{rl}/v_l) + (k_{rg}/v_g)} \quad [15]$$

Diffusion coefficient $$\rho D^{k} = \rho_l s D^{k}_{l} + \rho_g(1-s)D^{k}_{g} \quad [16]$$

Advection correction factor $$\gamma_c = \frac{\rho(\lambda_l C^{k}_{l} + \lambda_g C^{k}_{g})}{\rho_l s C^{k}_{l} + \rho_g(1-s)C^{k}_{g}} \quad [17]$$

Relative mobilities $$\lambda_l(s) = \frac{k_{rl}/v_l}{k_{rl}/v_l + k_{rg}/v_g}$$

$$\lambda_g(s) = 1 - \lambda_l(s) \quad [18]$$

Individual phase velocities

$$\rho_l\mathbf{u}_l = \mathbf{j}_l + \lambda_l\rho\mathbf{u} \quad [19]$$

$$\rho_g\mathbf{u}_g = -\mathbf{j}_l + \lambda_g\rho\mathbf{u} \quad [20]$$

where

$$\mathbf{j}_l = \frac{\lambda_l\lambda_g K\rho}{\mu}[\nabla p_c + (\rho_l - \rho_g)\mathbf{g}] \quad [21]$$

The reader is referred to the original references of the two-phase mixture model for further details of these model variables and their physical meanings.[36,37]

Constitutive relations.—The relative permeabilities for liquid and gas phases and the capillary pressure between the two phases are[36]

$$k_{rl} = s^3 \quad \text{and} \quad k_{rg} = (1-s)^3 \quad [22]$$

$$p_c = \sigma\cos\theta\left(\frac{\varepsilon}{K}\right)^{1/2}[1.417(1-s) - 2.120(1-s)^2 + 1.263(1-s)^3] \quad [23]$$

where the surface tension effect on capillary pressure is simply modified by contact angle, θ, with $\theta > 90°$ for hydrophobic surfaces and $\theta < 90°$ for hydrophilic surfaces.

Equilibrium conditions.—On the anode side, there are three components, *i.e.*, water, methanol, and carbon dioxide. In this gas-liquid coexisting system, local thermodynamic equilibrium prevails at the phase interface. Hence, the gas phase in the anode can be considered saturated with water and methanol vapors. It thus follows that

$$C^{H_2O}_{g,\text{sat}} = \frac{M^{H_2O}p^{H_2O}_{v,T}}{\rho_g RT} \quad [24]$$

where $p^{H_2O}_{v,T}$ is the water vapor saturation pressure obtainable from steam tables. Compared to Argyropoulos *et al.*[38] who used a set of complicated equations to calculate the vapor-liquid equilibrium state of methanol on the anode side, the Henry's law is simply applied here to calculate the methanol vapor pressure

$$p^{\text{MeOH}}_{v} = k_H x^{\text{MeOH}}_{l} \quad [25]$$

Table I. Physicochemical properties.

Parameter	Symbol	Value	Ref.
Diffusion coefficient of oxygen in gas	$D_g^{O_2}$	$1.775\left(\frac{T}{273}\right)^{1.823}\left(\frac{1.013\times10^5}{p}\right)$ m^2/s	Cussler[44]
Diffusion coefficient of carbon dioxide in gas	$D_g^{CO_2}$	3×10^{-5} m^2/s	Assumed
Diffusion coefficient of carbon dioxide in liquid	$D_l^{CO_2}$	1×10^{-10} m^2/s	Assumed
Diffusion coefficient of methanol in gas	D_g^{MeOH}	$\left(\begin{array}{c}-6.954\times10^{-2}+4.5986\\ \times10^{-4}T\\ +9.4979\times10^{-7}T^2\end{array}\right)\times10^{-4}$ m^2/s	Yaws[45]
Diffusion coefficient of methanol in liquid	D_l^{MeOH}	$10^{-5.4163-999.778/T}$ m^2/s	Yaws[45]
Diffusion coefficient of water in gas	$D_g^{H_2O}$	$2.56\times10^{-5}\left(\frac{T}{307}\right)^{2.334}\left(\frac{1.013\times10^5}{p}\right)$ m^2/s	Cussler[44]
Diffusion coefficient of water in liquid	$D_l^{H_2O}$	0 m^2/s	Assumed
Electro-osmotic drag coefficient of water	$n_d^{H_2O}$	2.5	Ren *et al.*[14]
Electro-osmotic drag coefficient of methanol	n_d^{MeOH}	$n_d^{H_2O}x^{MeOH}$	Ren *et al.*[14]
Henry's law constant	k^{MeOH}	$0.096e^{0.04511(T-273)}$ atm	Fitted from McGlashan and Williamson[46]
Viscosity of liquid water	μ_l	$0.458509-5.30474\times10^{-3}T+2.31231\times10^{-5}T^2-4.49161\times10^{-8}T^3+3.27681\times10^{-11}T^4$ kg/m s	Incropera and DeWitt[47]
Viscosity of gas	μ_g	2.03×10^{-5} kg/m s	Incropera and DeWitt[47]
Proton conductivity of membrane	κ	0.123 S/cm	Ren *et al.*[9]
Thermodynamic potential of oxygen reduction	$U_o^{O_2}$	1.24 V	—
Thermodynamic potential of methanol oxidation	U_o^{MeOH}	0.03 V	—
Cathodic transfer coefficient of cathode	α_c	0.875	Fitted from Gottesfeld and Zawodzinski[47]
Anodic transfer coefficient of anode	α_a	0.239	Fitted from Ren *et al.*[9]
Reference exchange current density of anode at 80°C	$I_{0,ref,80°C}^{MeOH}$	94.25 A/m^2	Fitted from Ren *et al.*[9]
Reference exchange current density of anode	$I_{0,ref}^{MeOH}$	$I_{0,ref,80°C}^{MeOH}e^{35570/R(1/273+80-1/T)}$	Fitted from Gottesfeld and Wilson[26]
Reference exchange current density of cathode at 80°C	$I_{0,ref,80°C}^{O_2}$	0.04222 A/m^2	Fitted from Gottesfeld and Zawodzinski[48]
Reference exchange current density of cathode	$I_{0,ref}^{O_2}$	$I_{0,ref,80°C}^{O_2}e^{73200/R(1/273+80-1/T)}$	Parthasarathy *et al.*[49]
Reference oxygen concentration of cathode kinetics	$C_{g,ref}^{O_2}$	0.23 kg/kg	—
Reference gas density	$\rho_{g,ref}$	1.2 kg/m^3	—
Porosity of cathode backing layer	ε_{bC}	0.7	Measured
Porosity of anode backing layer	ε_{bA}	0.7	Measured
Porosity of membrane	ε_{mS}	0.3	Measured
Permeability of anode backing layer	K	1×10^{-11} m^2	Assumed
Permeability of cathode backing layer	K	1×10^{-11} m^2	Assumed

In this equation, the methanol vapor pressure is dependent on temperature and liquid-phase mole fraction. The Henry's law constant, k_H, is a function of temperature as listed in Table I, and the liquid-phase methanol molar fraction, x_l^{MeOH}, can be determined from the mass fraction for a dilute solution

$$x_l^{MeOH} \approx \frac{M^{H_2O}}{M^{HeOH}} C_l^{MeOH} \quad [26]$$

Hence, the methanol mass fraction in the gas phase is given by

$$C_g^{MeOH} = \frac{M^{MeOH} p_v^{MeOH}}{\rho_g RT} \quad [27]$$

The mass fractions of carbon dioxide in gas and liquid phases are simply given by

$$C_g^{CO_2} = \frac{M^{CO_2}(p - p_{v,T}^{H_2O} - p_v^{MeOH})}{\rho_g RT} \text{ and } C_l^{CO_2} = C_{l,sat}^{CO_2} \quad [28]$$

Finally, the liquid saturation in the anode backing layer can be calculated from

$$s = \frac{\rho_g(C^{CO_2} - C_g^{CO_2})}{\rho_l(C_{l,sat}^{CO_2} - C^{CO_2}) + \rho_g(C^{CO_2} - C_g^{CO_2})} \quad [29]$$

if $C^{CO_2} \geqslant C_{l,sat}^{CO_2}$. When $C^{CO_2} < C_{l,sat}^{CO_2}$, $s = 1$.

Liquid water appears in the cathode backing layer when the water vapor pressure reaches its saturated value corresponding to the operating cell temperature. Inside the two-phase zone, thermodynamic equilibrium is assumed to hold true similarly for the anode, and thus the mass fractions of water in gas and liquid phases are given by their equilibrium values, respectively. That is

$$C_{g,sat}^{H_2O} = \frac{M^{H_2O} p_{v,T}^{H_2O}}{\rho_g RT} \quad \text{and} \quad C_{l,sat}^{H_2O} = 1 \quad [30]$$

The liquid saturation in the cathode is therefore determined from the mixture concentration of water via the following relation

$$s = \frac{\rho_g(C^{H_2O} - C_{g,sat}^{H_2O})}{\rho_l(C_{l,sat}^{H_2O} - C^{H_2O}) + \rho_g(C^{H_2O} - C_{g,sat}^{H_2O})} \quad [31]$$

Similarly, oxygen and carbon dioxide mass concentrations in both phases on the cathode side are calculated from

$$C_{l,sat}^{O_2} = 0 \quad \text{and} \quad C_{g,sat}^{O_2} = \left[\frac{\rho_l s}{\rho_g(1 - s)} + 1\right] C^{O_2} \quad [32]$$

$$C_{l,sat}^{CO_2} = 0 \quad \text{and} \quad C_{g,sat}^{CO_2} = \left[\frac{\rho_l s}{\rho_g(1 - s)} + 1\right] C^{CO_2} \quad [33]$$

It is assumed that oxygen and carbon dioxide are insoluble in the liquid phase on the cathode side.

Within the PEM separator, the membrane is assumed to be fully hydrated with liquid, thus

$$s = 1 \quad \text{for} \quad H_{cm} \leqslant y \leqslant H_{ma} \quad [34]$$

The complicated two-phase hydrodynamics at the channel/backing interface makes the liquid saturation at this interface difficult to determine theoretically so that an empirical approach is taken in this paper. In principle, the interface saturation is equal to unity at zero current density but zero at an infinitely large current density. It follows that

$$s|_{y=H_{af}} = \frac{1}{1 + aI} \quad [35]$$

where a is a coefficient to be calibrated by flow visualization experiments. According to the most recent flow visualization,[50] the interfacial saturation is estimated to be about 0.9 at a current density of 0.2 A/cm^2. This results in $a = 0.556\ (\text{A/cm}^2)^{-1}$.

Fluid channels

Governing equations.—Continuity: The most recent flow visualization study revealed that the two-phase flow pattern in the anode channel ranges from homogeneous to slug flow depending on the backing layer material, *i.e.*, whether carbon cloth or carbon paper.[51] For both flow patterns, it is more appropriate to consider a one-dimensional flow and transport model along the flow direction that is averaged over the cross section of the channel. In addition, it can be assumed that there is thermodynamic equilibrium and the phase-change effects on two-phase flow are negligible in the channels. A drift-flux model is thus used in the present work to describe the significant gas-liquid two-phase flow in the anode channel. Details are presented below.

For the anode channel, the continuity equations for both phases can be written as

$$\frac{d}{dx}[\rho_l U_l(1 - \alpha)] = -\frac{N_l}{H_{cA}} \quad [36]$$

$$\frac{d}{dx}[\rho_g U_g \alpha] = -\frac{N_g}{H_{cA}} \quad [37]$$

where U_l and U_g are phase velocities of liquid and gas averaged across the flow channel, respectively, and α is the void fraction (*i.e.*, the gas volume fraction). The terms N_l and N_g stand for mass exchange fluxes of liquid and gas between the channel and backing layer. Based on the drift flux model for the two-phase flow in a channel,[39,40] one has the following relationship between the gas and liquid phase velocities

$$U_g = C_0[\alpha U_g + (1 - \alpha)U_l] + U_{gj} \quad [38]$$

where C_0 is a distribution parameter and U_{gj} is the drift flux velocity. According to Wolk *et al.*,[39] the distribution parameter and drift flux velocity for the slug flow through rectangular channels are given by

$$C_0 = 1.35 - 0.35\sqrt{\frac{\rho_g}{\rho_l}} \quad [39]$$

and

$$U_{gj} = \left(0.23 + 0.13\frac{H_s}{H_w}\right)\sqrt{\frac{(\rho_l - \rho_g)g_x H_w}{\rho_l}} \quad [40]$$

Note that in Eq. 40 the drift flux velocity is caused by buoyancy forces of the gas phase relative to liquid. On the other hand, the study of Triplett *et al.*[41] showed that the homogeneous model is more accurate for the two-phase flow through microcapillary tubes. Fukano and Kariyasaki[42] also noted that the homogeneous model is true for two-phase flow because the tube diameter is smaller than 5.6 mm. In such a case, the two phase velocities are equal, and the distribution parameter and drift-flux velocity become unity and zero, respectively, in Eq. 38. Therefore, the homogeneous model is a limiting case of the drift flux model. Because two-phase flow patterns in the DMFC anode have yet to be established quantitatively, all the numerical results to be presented in the following are obtained with the homogeneous flow.

Due to a relatively small fraction of liquid droplets present in the cathode gas channel (*i.e.*, mist flow), the two-phase effect is neglected therein. Hence only the gas flow is considered as far as hydrodynamics is concerned.

Species conservation:

For species transport in the anode flow channel, one has

$$\frac{d}{dx}[\rho_l U_l(1-\alpha)\overline{C}_l^k] + \frac{d}{dx}[\rho_g U_g \alpha \overline{C}_g^k] = -\frac{\rho_l v_l C_l^k|_{y=H_{af}} + h_{ml}^k \rho_l(\overline{C}_l^k - C_l^k|_{y=H_{af}})}{H_{cA}} - \frac{\rho_g v_g C_g^k|_{v=H_{af}} + h_{mg}^k \rho_g(\overline{C}_g^k - C_g^k|_{v=H_{af}})}{H_{cA}}. \quad [41]$$

where the right side of Eq. 41 describes the species transfer rate due to fluid convection and species diffusion at the channel/backing interface. Along the channel/backing interface, the cross-sectional area fraction of two-phase interface is much smaller than that of the single-phase fraction, *i.e.*, gas-gas and liquid-liquid phase interface, therefore, the species transfer between gas and liquid phases at the channel/backing interface is neglected in this paper. The mass-transfer coefficients used in this equation refer to a permeable surface and therefore are rather complicated. Their expressions for similar situations were developed by Irandoust and Andersson[43] for Taylor flow in a circular capillary tube of monolithic catalyst reactors. These correlations are used in the present model for DMFC as a first approximation before more relevant and accurate relations become available. Hence

$$h_{ml}^k = Sh_l \frac{D_{l,eff}^k}{H_{cA}} \quad [42]$$

$$h_{mg}^k = Sh_g \frac{D_{g,eff}^k}{H_{cA}} \quad [43]$$

$$Sh_l = 1.5 \times 10^{-7} Re^{1.648} Sc^{0.177} \left(\frac{\delta_{film}}{H_{cA}}\right)^{-0.2338} \quad [44]$$

$$Sh_g = \frac{\delta_{film}}{H_{cA}} \quad [45]$$

where the thickness of the liquid film around a Taylor bubble in the circular capillary channel is given by

$$\frac{\delta_{film}}{H_{cA}} = 0.18[1 - \exp(-3.1 C_a^{0.54})] \quad [46]$$

with the capillary number defined as

$$C_a = \frac{\mu_l|\alpha U_g + (1-\alpha)U_l|}{\sigma} \quad [47]$$

The effective diffusion coefficients of gas and liquid phases in the channel are dependent on the gas-phase void fraction and phase distribution in the channel. As a result, the following equations are used to describe these two coefficients

$$D_{l,eff}^k = \frac{(1-\alpha)D_l^k}{\tau_l} \quad [48]$$

$$D_{g,eff}^k = \frac{\alpha D_g^k}{\tau_g} \quad [49]$$

where τ_l and τ_g are tortuosity factors for liquid- and gas-phase species transfer in the channel.

Alternatively, the mass-transfer coefficients between the anode backing and channel can be simply obtained using the effective diffusion coefficient of each phase with a fully developed flow[36] in which the Sherwood number for both gas and liquid phases in Eq. 42 and 43 are given by

$$Sh = 2.693 \quad [50]$$

As a first step, Eq. 42, 43, and 50 have been used in this work.

There is predominant gas flow through the cathode channel. As such, the species balance equation for the gas phase can be similarly written as

$$\frac{d}{dx}[\rho_g U_g \overline{C}_g^k] = -\frac{\rho_g v_g C_g^k|_{y=0} + h_{mg}^k \rho_g(\overline{C}_g^k - C_g^k|_{y=0})}{H_{cC}} \quad [51]$$

where

$$h_{mg}^k = Sh \frac{D_g^k}{H_{cC}} \quad [52]$$

and the Sherwood number can be obtained by Eq. 50.

Inlet and outlet boundary conditions.—At the channel inlet, velocity and species concentrations are prescribed as

$$U_g|_{x=0} = U_{in,C} \quad [53]$$

$$\overline{C}_g^k|_{x=0} = C_{g,in,C}^k \quad [54]$$

for the gas-feed cathode fluid channel, and

$$U_l|_{x=0} = U_{in,A} \quad [55]$$

$$\overline{C}_l^k|_{x=0} = C_{l,in,A}^k \quad [56]$$

for the liquid-feed anode fluid channel. As use is made of the one-dimensional flow and transport model averaged over the channel cross section, no boundary condition is required for the channel outlets. On all other boundary surfaces, no-flow and no-flux are applied; that is

$$\left.\frac{\partial p}{\partial x}\right| = 0 \quad \left.\frac{\partial C^k}{\partial x}\right| = 0 \quad [57]$$

Electrochemical kinetics.—According to Ren *et al.*,[22] methanol oxidation is a zero-order reaction when the methanol concentration is higher than 0.1 M. In this work, a Tafel kinetic equation for methanol oxidation is developed by fitting the experimental data from Ren *et al.*[9] as follows

$$I = I_0^{MeOH} \exp\left(\frac{\alpha_a F}{RT}\eta_a\right) \quad [58]$$

As the methanol concentration at the reaction surface is lower than a threshold value, a first-order reaction is considered in this paper. Therefore, the exchange current density in Eq. 58 is expressed as

$$I_0^{MeOH} = I_{0,ref}^{MeOH}\left(\frac{c_l^{MeOH}}{c_{l,threshold}^{MeOH}}\right)^n \quad [59]$$

$$n = \begin{cases} 0; & (c_l^{MeOH} \geqslant c_{l,threshold}^{MeOH}) \\ 1; & (c_l^{MeOH} < c_{l,threshold}^{MeOH}) \end{cases} \quad [60]$$

where the threshold methanol concentration, $c_{l,threshold}^{MeOH}$, is set at 0.1 M.

Tafel kinetics of the first order is employed to describe the reaction current of oxygen reduction on the cathode catalyst interface, namely

$$I + I_p = I_{0,ref}^{O_2} \frac{(1-s)\rho_g C_g^{O_2}|_{v=H_{cm}}}{\rho_{g,ref} C_{g,ref}^{O_2}} \exp\left(-\frac{\alpha_c F}{RT}\eta_c\right) \quad [61]$$

where the term $(1-s)$ is used to account for the fraction of surface rendered inactive by the presence of liquid water and the parasitic current density on the left side of Eq. 61 is attributed to oxidation of methanol crossing the membrane as given by Eq. 9. Note that the

Table II. Base case and its operating conditions.

Parameter	Symbol	Value
Cathode backing thickness	H_{bC}	0.03 cm
Anode backing thickness	H_{aA}	0.03 cm
PEM thickness	H_{mS}	0.0185 cm
Anode channel height	H_{cA}	0.2 cm
Cathode channel height	H_{cC}	0.2 cm
Cell length	L	7 cm
Operating temperature	T	80°C
Cathode channel pressure	p_C	1 atm
Anode channel pressure	p_A	1 atm
Inlet velocity of cathode channel	$U_{in,C}$	0.2 m/s
Inlet velocity of anode channel	$U_{in,A}$	0.0006 m/s
Inlet relative humidity at cathode	RH_{in}	3.43%
Inlet oxygen concentration at cathode	$C^{O_2}_{g,in,C}$	0.23 kg/kg (0.21 mol/mol)
Inlet methanol concentration at anode	$C^{MeOH}_{l,in,A}$	0.032 kg/kg (1 M)
Contact resistance	$R_{contact}$	0 Ω cm^2

term $(1 - s)$ is only a simplification to account for the flooding effect, because it remains unknown exactly how liquid water blocks the triple access (gas reactant, electrons, and protons) to each active catalyst site and hence reduces the oxygen reduction reaction surface.

Cell voltage.—Once values of the anode and cathode overpotential are calculated, the cell voltage can be determined as follows

$$V_{cell} = U_o^{O_2} - U_o^{MeOH} - \eta_a + \eta_c - I\frac{H_{mS}}{\kappa} - IR_{contact} \quad [62]$$

where $U_o^{O_2}$ and U_o^{MeOH} are the thermodynamic equilibrium potentials of oxygen reduction and methanol oxidation and their difference is not equal to the open-circuit voltage because the cathode surface overpotential is nonzero even under open circuit in order to sustain the parasitic current from methanol crossover. The proton conductivity κ is assumed to be a constant since the membrane is fully hydrated in liquid-feed DMFC. The last term in Eq. 62 denotes the ohmic loss due to contact resistances between mating cell components.

Numerical Results

Baseline case.—Using a CFD technique, the present model is numerically solved for a two-dimensional liquid-feed DMFC under the baseline conditions listed in Table II.

The predicted polarization curve of the baseline case is shown in Fig. 2 (*i.e.*, curve 1). In this simulation, anode and cathode flow rates correspond to the stoichiometric current densities of 1 and 1.6 A/cm^2, respectively. It can be seen that the open-circuit voltage is much lower than the thermodynamic equilibrium cell voltage (*i.e.*, 1.21 V) as a result of methanol crossover. This prediction is in accordance with experimental observations. In addition, the cell voltage drops very fast with increasing current density despite the fact that the ohmic drop in the fully hydrated membrane is quite small, *i.e.*, 150 mΩ cm^2 for Nafion 117. This is caused by the high Tafel slope of the methanol oxidation reaction in the anode catalyst layer, *i.e.*, 0.293 V/decade at 80°C in this baseline case. Finally it is shown that the cell current density is limited at 0.529 A/cm^2 by mass transport controlled by the anode feed concentration of methanol and two-phase mass-transport resistance from the anode channel to the anode catalyst layer.

To elucidate the two-phase mass-transport effect on cell performance, the baseline cell is also simulated by considering the liquid-phase transport only in both the anode channel and backing. This hypothetical simulation was carried out using the same computer code with the liquid saturation in the anode backing and the void fraction in the anode channel deliberately set to unity and zero,

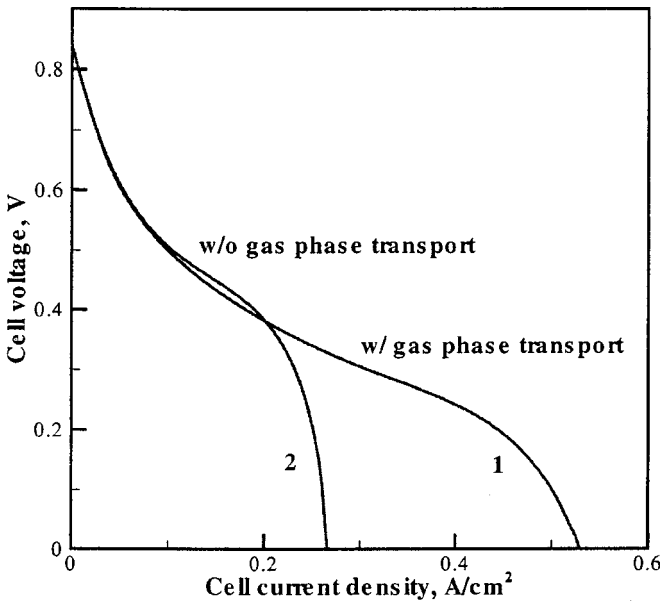

Figure 2. Polarization curves for the baseline cell with and without mass transport through the gas phase.

respectively, representative of only liquid-phase transport in the anode. The polarization curve in this case is shown in Fig. 2 as curve 2 and indicates a limiting current density of only 0.266 A/cm^2. The rather low limited current density due to slow methanol diffusion in liquid can be estimated by considering the feeding methanol concentration and the anode channel and backing mass transfer resistances using the following equation

$$I_{lim} = \frac{6Fj^{MeOH}_{max}}{M^{MeOH}} = 6F\frac{c_l^{MeOH}}{\frac{1}{h^{MeOH}_{ml,A}} + \frac{H_{bA}}{D^{MeOH}_{l,eff}}} \quad [63]$$

where the mass-transfer coefficient, $h^{MeOH}_{ml,A}$, can be calculated by Eq. 42 and 50 with a zero void fraction and the effective diffusion coefficient in the anode backing layer is obtained by Eq. 7 with both the liquid saturation and tortuosity factor equal to unity. The mass-transfer resistance between the fluid channel and backing layer is 1.7 times of that in the backing layer with 2 mm channel width while 0.6 times with 0.7 mm channel width. Both mass-transfer resistances are of the same magnitude and not negligible. At the methanol feed concentration of 1 M, the limiting current density is estimated by Eq. 63 to be 0.279 A/cm^2 in this baseline case of 2 mm channel width cell, closely matching the numerically predicted value. This means that cell current densities higher than 1 A/cm^2 that were reported in the experiments of Ren *et al.*[25] is impossible to sustain by methanol transport through the liquid phase only. Therefore, the gas phase is an important pathway for methanol to be transported to the reaction surface. The much-facilitated methanol transport through the gas phase is due to the fact that the diffusion coefficient in gas phase is nearly four orders of magnitude greater than that in liquid.

Figure 2 also shows that before reaching limiting currents, the cell voltage for the liquid transport case is slightly higher than that with the two-phase transport effects included. This is because the presence of the gas phase enhances the methanol transport in the anode, thereby resulting in more severe methanol crossover and hence voltage loss associated with it. Clearly, gas-phase diffusion is an important mechanism that cannot be neglected in the modeling of species transport in the liquid-feed DMFC anode. Notice also the sharp drop of the cell voltage in the mass-transport controlled regime shown in Fig. 2, which coincides with the shift of methanol

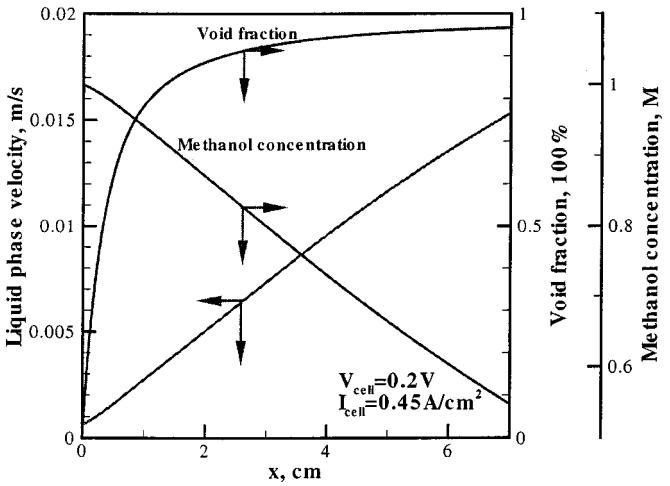

Figure 3. Axial profiles of the liquid-phase velocity, void fraction, and average methanol concentration in the anode channel at 0.45 A/cm^2.

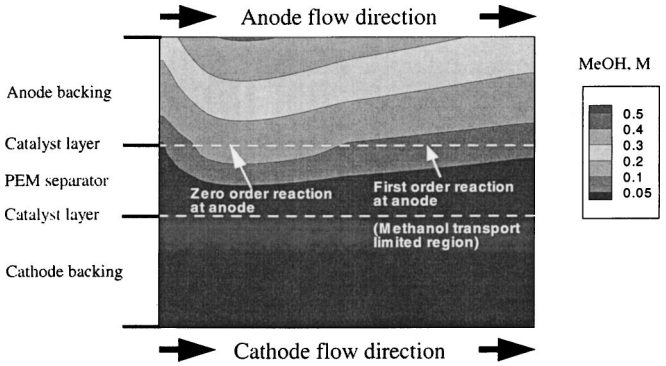

Figure 4. Methanol concentration contours in the membrane-electrode assembly for 0.45 A/cm^2.

oxidation reaction from zero order to the first order. There is no concentration polarization on the anode until the methanol concentration at the catalyst site decreases to 0.1 M.

In practical DMFC systems, the anode liquid is recovered through a gas-liquid separator. As such, the inlet methanol solution is saturated with dissolved CO_2, and gas bubbles would appear immediately in the anode channel as soon as current is drawn on the cell. Figure 3 shows the axial distributions of several flow parameters in the anode channel for the cell current density of 0.45 A/cm^2. According to Fukano and Kariyasaki,[42] the gravitational effect on the two-phase flow in a minichannel is negligible as compared to the surface tension, implying that the homogeneous model for the anode channel flow is more appropriate, which is used in the present simulation. Thus, the liquid-phase velocity shown in Fig. 3 also represents the gas-phase velocity. The velocity increases along the flow direction due to volume expansion of the two-phase mixture. The nearly uniform current density distribution, as discussed below, leads to a linear increase of phase velocity. At the channel outlet, the phase velocity reaches 0.015 m/s, 25 times the inlet velocity, 6×10^{-4} m/s.

The void fraction in the anode channel increases rapidly along the flow direction, especially in the region near the inlet as shown in Fig. 3. The void fraction increases from 0% at the inlet to 80% within one-seventh of the length into the channel and roughly 95% at the outlet. The void fraction greatly affects the overall mass transfer between the channel and backing layer according to Eq. 41, 42, 43, 48, and 49 since the gas-phase diffusion coefficient is four orders of magnitude higher than the liquid. With the increase in void fraction, the mass transfer between the anode channel and backing is significantly augmented. As a result, the overall mass-transfer resistance from the anode channel to the backing layer decreases along the flow direction, which influences the methanol supply from the anode channel to the backing and then the methanol concentration distribution discussed in the following figure.

Figure 3 also shows the average methanol concentration distribution in the liquid phase of the anode channel. It decreases almost linearly from 1 to 0.55 M along the flow direction due to the electrochemical consumption at the anode catalyst layer and the methanol crossover to the cathode. Hence, the stoichiometric flow ratio of methanol supply is 2.2 at the anode in this case. At this high current density, most of the methanol lost from the anode solution is consumed for producing the cell current, and there is minimal methanol crossover occurring. It should be also noted that the gas phase at the anode outlet contains a quite bit of methanol due to the combination of relatively high methanol concentration in the gas phase, high gas-phase velocity, and high void fraction. Thus recycling the gas-phase methanol seems to be necessary for high fuel utilization.

Figure 4 shows the methanol concentration contours in the anode and cathode backing layers and the PEM under the same operating conditions as in Fig. 3. Near the inlet, the overall mass-transfer coefficient increases steeply due to the rapid increase in the gas-phase volume fraction, causing a quick increase of the methanol concentration at the channel/backing interface. In the remaining portion of the cell, the overall mass-transfer coefficient varies slightly due to a relatively slow change in the void fraction within the anode channel. Thus the methanol depletion along the axial direction of the channel dominates the variation of the methanol concentration along the anode channel/backing interface. In the middle portion of the anode, the methanol concentration at the anode catalytic surface is higher than 0.1 M so that a zero-order reaction of methanol oxidation occurs, while in portions near the inlet and outlet, the methanol concentration is lower than the threshold concentration, 0.1 M, implying a first-order reaction at the anode catalyst. In the first-order reaction region as illustrated in Fig. 4, there is a limitation in methanol transport and minimal methanol crossover results. The methanol concentration distribution in the membrane is the result of methanol transport by diffusion, electro-osmotic drag, and convection. The methanol concentration in the cathode is essentially equal to zero because any methanol crossed over through the membrane is immediately oxidized into CO_2.

Figure 5 displays the current density distribution along the flow direction under the same base conditions. In accordance with Fig. 4, the local current density profile features two mass-transport-limited regions close to the inlet and outlet, respectively, where the local current density is lower than that in the middle region.

Methanol crossover.—Methanol crossover is driven by diffusion, pressure gradient caused convection, and electro-osmosis. The three contributors manifest differently under different operating conditions. Figures 6a and b show the axial distributions of the total methanol crossover flux and its individual contributors for cases of a high and a low current densities, respectively. Figure 6a corresponds to the baseline cell operation with the current density of 0.45 A/cm^2. In this high cell current density case, methanol crossover occurs only in the middle portion of the cell, where the contributions of diffusion and electro-osmosis equally dominate while the convection contribution is absent due to no pressure gradient between the anode and cathode chambers. The variation of the net methanol crossover flux along the flow direction in this figure explains the current density distribution shown in Fig. 5.

Figure 6b shows the various contributions to methanol crossover at the cell current density of 0.18 A/cm^2. In this low current density case, diffusion dominates the net methanol crossover at all locations. The contribution of electro-osmosis accounts for 15% of the net crossover flux. Compared to Fig. 6a, the maximum diffusion flux is increased from about 0.037 to 0.09 A/cm^2 due to the significant rise of methanol concentration at the anode catalyst layer.

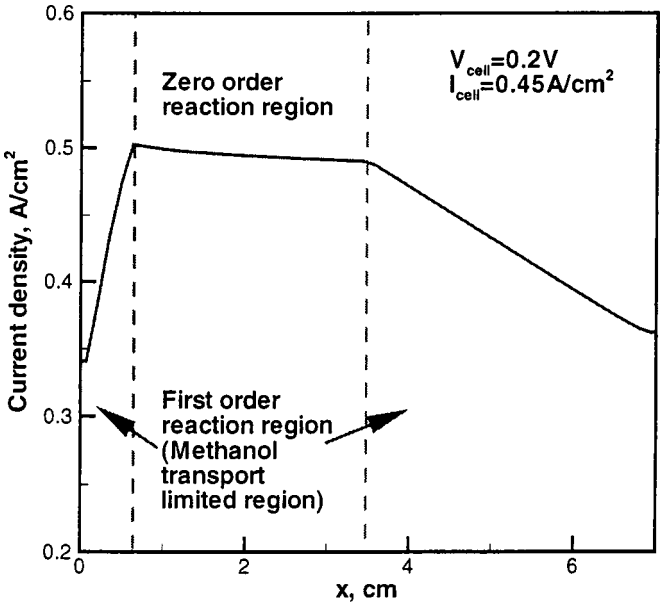

Figure 5. Local current density distribution in the flow direction for the average cell current density of 0.45 A/cm^2.

At open circuit, no current is drawn from the anode and the anode fluid is in the liquid state. Hence methanol transport occurs only by liquid diffusion from the anode channel, to the anode backing layer, then through the membrane separator to the cathode catalyst layer. The methanol crossover flux can thus be estimated by the following equation

$$I_{p,oc} = \frac{6Fj_{max}^{MeOH}}{M^{MeOH}} = 6F\frac{c_l^{MeOH}}{\frac{1}{h_{ml,A}^{MeOH}} + \frac{H_{bA}}{D_{l,eff,bA}^{MeOH}} + \frac{H_{mS}}{D_{l,eff,mS}^{MeOH}}} \quad [64]$$

Using the membrane tortuosity factor of 1.8 and the backing layer tortuosity factor and liquid saturation of unity, Eq. 64 gives a methanol crossover current density of 0.116 A/cm^2 at 80°C and open circuit.

The detrimental effect of methanol crossover on cell performance can be seen from Fig. 7 that shows the polarization curves with and without methanol crossover. At small current densities, the cell voltage difference can be as high as 0.1 V. This voltage loss diminishes with the current density and becomes zero when reaching its mass-transport limiting current density. At this point no methanol crosses through the membrane and nearly all the methanol is consumed by anode oxidation. It is noted, however, that the predicted cell voltage loss due to methanol crossover appears to be less significant than that observed experimentally. Further work is needed to fully explain this.

Figure 8 shows the effects of cell temperature on the methanol crossover flux at different cell current densities. The methanol crossover current increases greatly with the cell temperature at the same operating current density. The maximum methanol crossover flux is about 0.05 A/cm^2 at 40°C but 0.15 A/cm^2 at 90°C. This is due to the increase in the methanol diffusion coefficient of the liquid phase as listed in Table I. It is interesting to note that the maximum crossover flux occurs at open circuit for temperatures between 40 and 80°C but at about 0.1 A/cm^2 at 90°C. This is due to the gas-phase transport contribution to methanol supply from the anode channel to the anode catalyst layer. For each case, methanol crossover flux decreases almost linearly with cell operating current density. At the mass-transport-limited current density, the methanol crossover flux is reduced to zero. The slope of each curve in Fig. 8 is dependent on the two-phase transport properties of methanol from the anode channel through the anode backing layer to the anode catalyst layer.

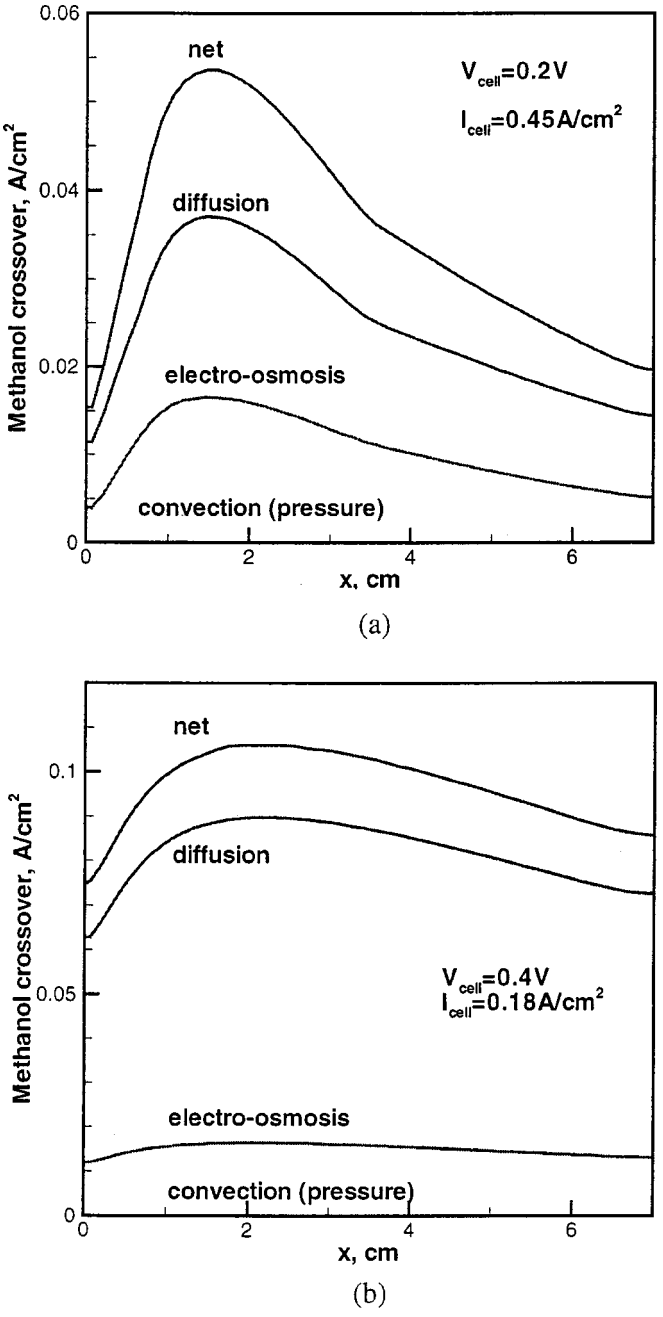

Figure 6. Axial distributions of methanol crossover flux and its contributors for (a) the high current density case and (b) the low current density case.

Effects of methanol feed concentration.—Figure 9 shows the effects of methanol feed concentration on the polarization curves under the operating conditions listed in Table II. The anode stoichiometric flow rate corresponds to $1 \times n$ A/cm^2, where n is the methanol feed concentration in the unit of M (mol/L). Better cell performance is achieved with low feed concentrations for small current densities because the rate of methanol crossover is minimized. However, operating with small feed concentrations suffers from low limiting current densities. Operation in the medium current density range requires a high methanol feed concentration, although its cell voltage is low at open circuit or low current densities because of excessive methanol crossover. The polarization curves for methanol

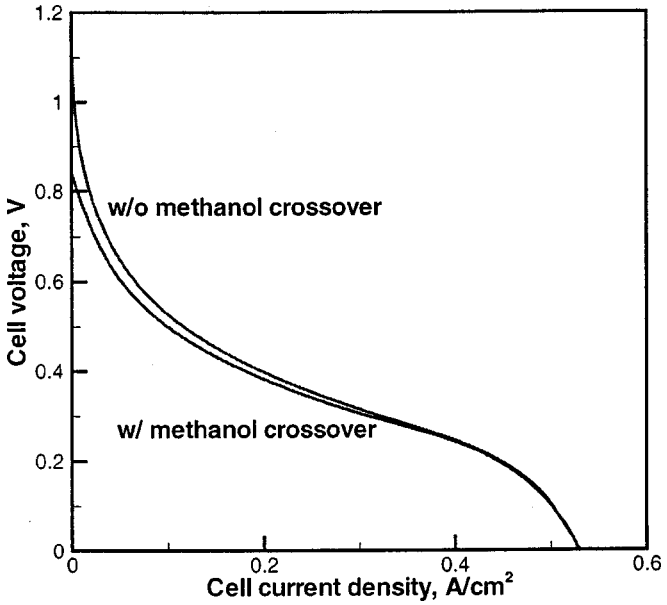

Figure 7. Methanol crossover effect on the polarization curve.

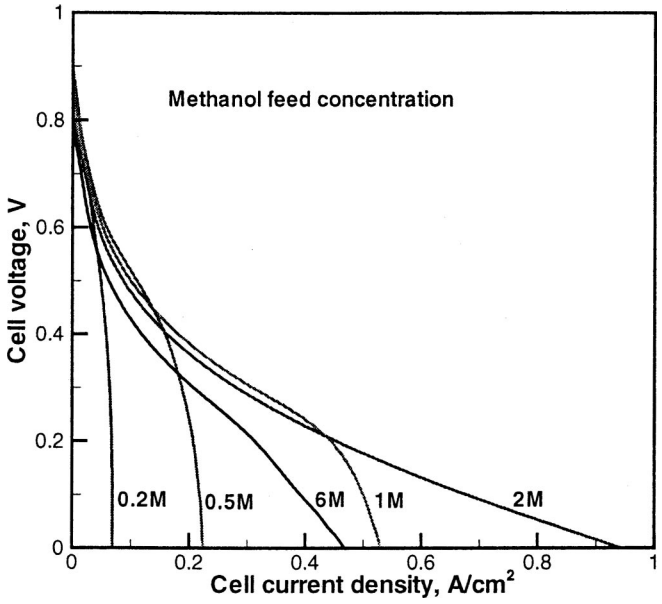

Figure 9. Polarization curves with different methanol feed concentrations.

feed concentrations higher than 1 M exhibit a different shape. In the presence of substantial methanol crossover experienced in high methanol feed concentration cases, say 6 M, a significant amount of oxygen in the cathode is consumed by methanol oxidation. Whereas the cell current density is limited by methanol mass transport with a smaller methanol feed concentration, the cell current density is limited by oxygen supply at a higher methanol feed concentration. While a stoichiometric flow ratio of the oxidant is traditionally defined on the basis of the net current density of the cell for convenience, it must be noted that the intrinsic stoichiometry of O_2 should be defined based on $(I + I_p)$. Under high current densities, the former stoichiometry is typically around 3 and 4, while the latter stoichiometry can be close to unity, meaning that the oxygen concentration at the outlet of the cathode is nearly zero.

Model validation.—The present model is validated by the experimental data of a 50 cm^2 stainless steel cell and a 5 cm^2 graphite cell. Figure 10 shows the polarization curves under two experimental conditions of the 50 cm^2 cell carried out by Mench *et al.*[23] In order to fit the experimental data, the reference anode exchange current density at 80°C and contact resistance used in the above simulation are adjusted in this part of the paper. The figure shows that the numerical results agree well if the contact resistance is 0.35 Ω cm^2 and the reference anode exchange current density is 28.3 A/m^2 for 80°C. The exchange current density in the present paper is defined on the basis of the electrode cross-sectional area.

The model is also validated against the experimental data of a 5 cm^2 graphite DMFC.[51] No contact resistance is assumed in this validation exercise and the anode exchange current density is chosen to be the same as listed in Table I. Figure 11 shows the polarization curves at two cell temperatures. Note that the anode kinetics of this cell was measured with the specific membrane-electrode assembly

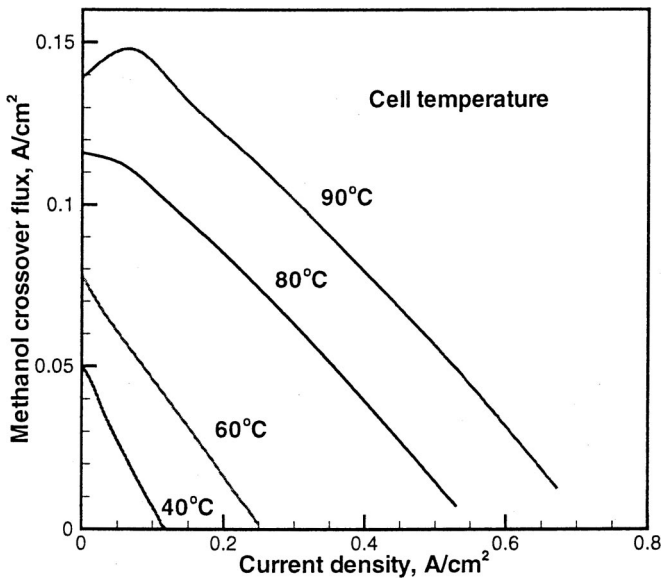

Figure 8. Methanol crossover flux as a function of cell current density and temperature.

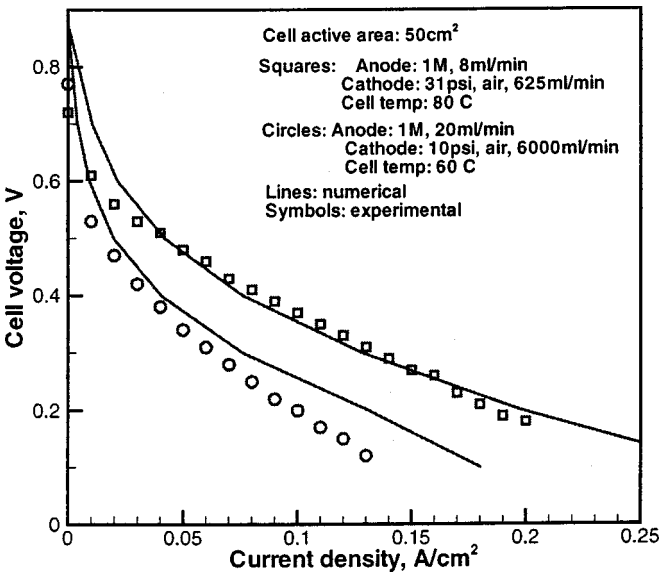

Figure 10. Validation of the present DMFC model against the experimental data of a 50 cm^2 stainless steel cell at two different temperatures.

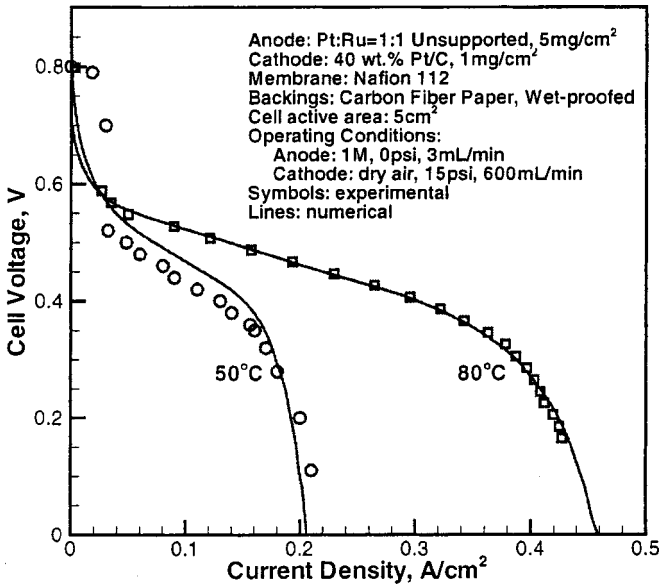

Figure 11. Validation of the present DMFC model against the experimental data of a 5 cm^2 cell at different temperatures.

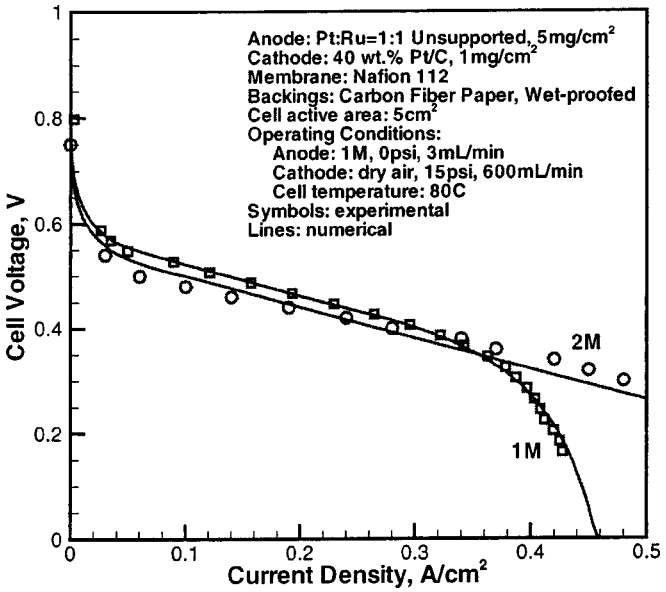

Figure 12. Validation of the present DMFC model against the experimental data of a 5 cm^2 cell at different methanol feed concentrations.

and fitted by the experimental data. The figure shows that the model predictions agree well with the experimental *I-V* curves. A lower mass-transport limited current density at 50°C is caused by the lower diffusion coefficients in both liquid and gas phases and the lower saturated methanol concentration in the gas phase at lower temperatures, which is due to a lower Henry's law constant as listed in Table II.

Figure 12 shows the predicted and experimental polarization curves for the 5 cm^2 cell at different methanol feed concentrations. In agreement with the experiments, the model prediction for the 2 M case shows a lower performance, due primarily to higher methanol crossover. No mass-transport limitation was found in either experiments and numerical calculations at this high methanol feed concentration condition.

Conclusions

A two-phase multicomponent model with mixed potential effects has been developed for the liquid-feed DMFC. Diffusion and convection of both gas and liquid phases are considered to more accurately predict methanol crossover through the membrane caused by diffusion, convection, and electro-osmosis. The model is solved numerically using computational fluid dynamics and validated against available experimental data. The interactive transport phenomena and electrochemical kinetics in liquid-feed DMFC are studied based on the simulation results, and the effects of methanol feed concentrations on cell performance are discussed. Gas-phase transport is important in delivering methanol to the reaction site due to its much higher diffusion coefficient. The void fraction at the outlet can be as high as 95% and the gas and liquid phase velocities in the anode can be increased by an order of magnitude from the inlet to the outlet due to significant volume expansion. The increase in methanol feed concentration leads to a slight decrease in cell voltage and a proportional increase in the maximum current density, when the methanol concentration is smaller than 1 M. At methanol concentrations greater than 2 M, the cell voltage is greatly reduced due to excessive methanol crossover and the maximum cell current density may be limited by oxygen transport on the cathode because the parasitic reaction of crossed methanol consumes oxygen as well. This also implies that the cathode stoichiometric flow ratio cannot be at a similarly low level to the hydrogen fuel cell not only because of the need to prevent cathode flooding but also the competing consumption of oxygen between parasitic and main cathode reactions.

Methanol crossover is dominated by molecular diffusion at zero and small current densities, and its flux distribution is nearly uniform along the flow direction. At high current densities, the methanol crossover flux becomes small and both the diffusion and electro-osmosis equally contribute to methanol crossover. The cell voltage can be reduced by 0.1 V with methanol crossover at a small current density, but the effect diminishes with the cell current density. With the increase of cell temperature, the methanol crossover flux increases greatly.

Acknowledgments

This research is partly funded by the Pennsylvania Department of Environmental Protection and The United States Department of Transportation Advanced Vehicle Program, and partly by Conoco-DOE Ultra-Clean Fuel Project under DOE Cooperative Agreement no. DE-FC26-01NT41098.

The Pennsylvania State University assisted in meeting the publication costs of this article.

List of Symbols

c	molar concentration, M
C	mass fraction, kg/kg
C_a	capillary number
C_0	distribution parameter
D	diffusivity, cm^2/s
F	Faraday constant, 96,487 C/mol
g	gravitational acceleration, cm/s^2
H_{af}	location of anode backing/channel interface, cm
H_{bA}	thickness of anode backing layer, cm
H_{bC}	thickness of cathode backing layer, cm
H_{cA}	anode channel height, cm
H_{cC}	cathode channel height, cm
H_{cm}	location of cathode backing/membrane interface (cathode catalyst layer), cm
h_m	mass-transfer coefficient between porous electrode and gas channel, cm/s
H_{ma}	location of membrane and anode backing interface (anode catalyst layer), cm
H_{mS}	membrane separator thickness, cm
H_s	length of shorter side of rectangular channel cross section, cm
H_w	length of wider side of rectangular channel cross section, cm
I	current density, A/cm^2
I_0	effective exchange current density, A/cm^2
I_p	parasitic current density at cathode resulting from methanol crossover, A/cm^2
$\mathbf{I}_e$	ionic current density vector, A/cm^2
j	species mass flux, kg/cm^2 s
K	permeability of porous material, cm^2
k_H	Henry's law constant, Pa
k_{rg}	relative permeability of gas phase

k_{rl}	relative permeability of liquid phase
L	cell length, cm
$\dot{m}$	source term in species conservation equation, kg/cm^3 s
M	molecular weight, kg/mol
M_k	formula of species k
N	mass flow rate, kg/cm^2 s
n_{Ri}	net electrode output of electrode reaction Ri
n_d	electro-osmotic drag coefficient
p	pressure, Pa
p_A	anode pressure, Pa
p_c	capillary pressure, Pa
p_C	cathode pressure, Pa
p_v	saturated vapor pressure, Pa
R	gas constant, J/(mol·K)
$R_{contact}$	ohmic contact resistance, Ω cm^2
Re	Reynolds number, $\rho u H/\mu$
RH	relative humidity
S^k_{Ri}	stoichiometric coefficient of species k in reaction Ri
Sc	Schmidt number, v/D
Sh	Sherwood number, $h_m H/D$
s	liquid saturation
t	time, s
T	temperature, K
U	phase velocity in channel, cm/s, or potential, V
$U_{g,j}$	drift velocity, cm/s
$\mathbf{u}$	superficial velocity vector, cm/s
u	velocity in x direction, cm/s
v	velocity in y direction, cm/s
V_{cell}	cell voltage, V
x	coordinate, cm, or mole fraction in liquid solution, mol/mol
y	coordinate, cm

Greek

α	void fraction in channel
α_a	anodic transfer coefficient at anode
α_c	cathodic transfer coefficient at cathode
γ_c	two-phase convection correction coefficient
δ_{film}	liquid film thickness of Taylor flow, cm
ε	porosity
η	overpotential, V
κ	ionic conductivity of membrane, cm/Ω
λ	relative mobility
μ	viscosity, kg/(cm·s)
ν	kinetic viscosity, cm^2/s
θ	contact angle, °
ρ	density, kg/cm^3
ρ_k	kinetic density, kg/cm^3
σ	interfacial tension, N/cm
τ	tortuosity factor in the anode channel

Superscripts

CO_2	carbon dioxide
H_2O	water
k	species k
MeOH	methanol
n	reaction order
O_2	oxygen
t_g	tortuosity factor of gas-phase diffusion in porous region
t_l	tortuosity factor of liquid phase diffusion in porous region
-	average value in channel

Subscripts

A	anode
bA	anode backing layer
bC	cathode backing layer
C	cathode
cA	anode channel
cC	cathode channel
eff	effective value
eq	equilibrium value
g	gas phase
in	inlet
l	liquid phase
mS	membrane separator
oc	open circuit
ref	reference value
sat	saturated

References

1. G. T. Burstein, C. J. Barnett, A. R. Kucernak, and K. R. Williams, *Catal. Today*, **38**, 425 (1997).
2. S. Wasmus and A. Kuver, *J. Electroanal. Chem.*, **461**, 14 (1999).
3. W. F. Lin, J. T. Wang, and R. F. Savinell, *J. Electrochem. Soc.*, **144**, 1917 (1997).
4. A. Hamnett, *Catal. Today*, **38**, 445 (1997).
5. S. C. Thomas, X. Ren, and S. Gottesfeld, *J. Electrochem. Soc.*, **146**, 4354 (1999).
6. L. Liu, C. Pu, R. Viswanathan, Q. Fan, R. Liu, and E. S. Smotkin, *Electrochim. Acta*, **43**, 3657 (1998).
7. E. Hayden, *Catal. Today*, **38**, 473 (1997).
8. T. Page, R. Johnson, J. Hormes, S. Noding, and B. Rambabu, *J. Electroanal. Chem.*, **485**, 34 (2000).
9. X. Ren, T. E. Springer, and S. Gottesfeld, *J. Electrochem. Soc.*, **147**, 92 (2000).
10. S. Arico, P. Creti, E. Modica, G. Monforte, V. Baglio, and V. Antonucci, *Electrochim. Acta*, **45**, 4319 (2000).
11. M. K. Ravikumar and A. K. Shukla, *J. Electrochem. Soc.*, **143**, 2601 (1996).
12. S. R. Narayanan, H. Frank, B. Jeffries-Nakamura, M. Smart, W. Chun, G. Halpert, J. Kosek, and C. Cropley, in *Proton Conducting Membrane Fuel Cells I*, S. Gottesfeld, G. Halpert, and A. Landgrebe, Editors, PV 95-23, p. 278, The Electrochemical Society Proceedings Series, Pennington, NJ (1995).
13. X. Ren, T. A. Zawodzinski, Jr., F. Uribe, H. Dai, and S. Gottesfeld, in *Proton Conducting Membrane Fuel Cells I*, S. Gottesfeld, G. Halpert, and A. Landgrebe, Editors, PV 95-23, p. 284, The Electrochemical Society Proceedings Series, Pennington, NJ (1995).
14. X. Ren, T. E. Springer, T. A. Zawodzinski, and S. Gottesfeld, *J. Electrochem. Soc.*, **147**, 466 (2000).
15. V. Tricoli, N. Carretta, and M. Bartolozzi, *J. Electrochem. Soc.*, **147**, 1286 (2000).
16. T. I. Valdez and S. R. Narayanan, in *Proton Conducting Membrane Fuel Cells II*, S. Gottesfeld, T. F. Fuller, and G. Halpert, Editors, PV 98-27, p. 380, The Electrochemical Society Proceedings Series, Pennington, NJ (1998).
17. S. Hikita, K. Yamane, and Y. Nakajima *JSAE Rev.*, **22**, 151 (2000).
18. J. T. Wang, S. Wasmus, and R. F. Savinell, *J. Electrochem. Soc.*, **143**, 1233 (1996).
19. P. S. Kauranen and E. Skou, *J. Electroanal. Chem.*, **408**, 189 (1996).
20. G. Halpert, S. R. Narayanan, T. Valdez, W. Chun, H. Frank, A. Kindler, S. Surampudi, J. Kosek, C. Cropley, and A. LaConti, in *Proceedings of the 32nd Intersociety Energy Conversion Engineering Conference*, Vol. 2, p. 774, AIChE, New York (1997).
21. M. Baldauf and W. Preidel, *J. Power Sources*, **84**, 161 (1999).
22. X. Ren, P. Zelenay, S. Thomas, J. Davey, and S. Gottesfeld, *J. Power Sources*, **86**, 111 (2000).
23. M. Mench, S. Boslet, S. Thynell, J. Scott, and C. Y. Wang, in *Direct Methanol Fuel Cells*, The Electrochemical Society Proceedings Series, Pennington, NJ (2001). S. R. Narayanan, S. Gottesfeld, and T. Zawodzinski, Editors, PV 2001 4, p. 241, The Electrochemical Society Proceedings Series, Pennington, NJ (2001).
24. M. Mench and C. Y. Wang, *J. Electrochem. Soc.*, **150**, A79 (2003).
25. X. Ren, M. S. Wilson, and S. Gottesfeld, *J. Electrochem. Soc.*, **143**, L12 (1996).
26. S. Gottesfeld and M. S. Wilson, in *Energy Storage Systems for Electronics Devices*, T. Osaka and M. Datta, Editors, p. 487, Gordon and Breach Science Publishers, Singapore (2000).
27. S. F. Baxter, V. S. Battaglia, and R. E. White, *J. Electrochem. Soc.*, **146**, 437 (2000).
28. J.-T. Wang and R. F. Savinell, in *Electrode Materials and Processes for Energy Conversion and Storage*, S. Srinivasan, D. D. Macdonald, and A. C. Khandkar, Editors, PV 94-23, p. 326, The Electrochemical Society Proceedings Series, Pennington, NJ (1994).
29. A. Kulikovsky, J. Divisek, and A. A. Kornyshev, *J. Electrochem. Soc.*, **147**, 953 (2000).
30. A. A. Kulikovsky, *J. Appl. Electrochem.*, **30**, 1005 (2000).
31. H. Dohle, J. Divisek, and R. Jung, *J. Power Sources*, **86**, 469 (2000).
32. K. Scott, P. Argyropoulos, and K. Sundmacher, *J. Electroanal. Chem.*, **477**, 97 (1999).
33. K. Sundmacher and K. Scott, *Chem. Eng. Sci.*, **54**, 2927 (1999).
34. P. Argyropoulos, K. Scott, and W. M. Taama, *J. Appl. Electrochem.*, **30**, 899 (2000).
35. K. Sundmacher, T. Schultz, S. Zhou, K. Scott, M. Ginkel, and E. D. Gilles, *Chem. Eng. Sci.*, **56**, 333 (2001).
36. Z. H. Wang, C. Y. Wang, and K. S. Chen, *J. Power Sources*, **94**, 40 (2001).
37. C. Y. Wang and P. Cheng, *Adv. Heat Transfer*, **30**, 93 (1997).
38. P. Argyropoulos, K. Scott, and W. M. Taama, *Chem. Eng. J.*, **78**, 29 (2000).
39. T. Wilmarth and M. Ishii, *Int. J. Heat Mass Transf.*, **37**, 1749 (1994).
40. G. Wolk, M. Dreyer, and H. J. Rath, *Int. J. Multiphase Flow*, **26**, 1037 (2000).
41. K. A. Triplett, S. M. Ghiaasiaan, S. I. Abdel-Khalik, A. LeMouel, and B. N. McCord, *Int. J. Multiphase Flow*, **25**, 395 (1999).
42. T. Fukano and A. Kariyasaki, *Nucl. Eng. Des.*, **141**, 59 (1993).
43. S. Irandous and B. Anderson, *Comput. Chem. Eng.*, **13**, 519 (1989).
44. E. L. Cussler, *Diffusion: Mass Transfer in Fluid Systems*, Cambridge University Press, New York (1984).
45. C. L. Yaws, *Handbook of Transport Property Data: Viscosity, Thermal Conductivity, and Diffusion Coefficients of Liquids and Gases*, Gulf Pub Co, Houston, TX (1995).
46. M. L. McGlashan and A. G. Williamson, *J. Chem. Eng. Data*, **21**, 196 (1976).
47. F. D. Incropera and D. P. DeWitt, *Fundamentals of Heat and Mass Transfer*, John Wiley & Sons, Inc., New York (1985).
48. S. Gottesfeld and T. A. Zawodzinski, *Adv. Electrochem. Sci. Eng.*, **6**, 195 (1997).
49. A. Parthasarathy, S. Srinivasan, A. J. Appleby, and C. R. Martin, *J. Electrochem. Soc.*, **139**, 2530 (1992).
50. G. Lu and C. Y. Wang, Electrochemical Engine Center (ECEC) Technical Report No. 2002-04 The Pennsylvanic State University, University Park, PA (2002).
51. C. Lim and C. Y. Wang, *J. Power Sources*, **13**, 145 (2003).